A

A high frequency sampling monitoring system for environmental and structural applications. Part A: The hardware architecture

CESARE ALIPPI, ROMOLO CAMPLANI, CRISTIAN GALPERTI, ANTONIO MARULLO, MANUEL ROVERI, Dipartimento di Elettronica e Informazione, Politecnico di Milano, Italy

High frequency sampling is not a prerogative of high energy physics or machinery diagnostic monitoring only: critical environmental and structural health monitoring applications also have such a challenging constraint. Moreover, such unique design constraints are often coupled with the requirement of high synchronism among the distributed acquisition units, minimal energy consumption and large communication bandwidth. Such severe constraints led scholars to suggest wired centralised monitoring solutions, which have only recently been complemented with wireless technologies. This paper suggests a hybrid wireless-wired monitoring system combining the advantages of wireless and wired technologies within a distributed high-frequency-sampling framework. The suggested architecture satisfies the mentioned constraints, thanks to an ad-hoc design of the hardware, the availability of efficient energy management policies and up-to-date harvesting mechanisms. At the same time, the architecture supports adaptation capabilities by relying on the remote reprogrammability of key application parameters. The proposed architecture has been successfully deployed in the Swiss-Italian Alps to monitor the collapse of rock faces in three geographical areas.

Additional Key Words and Phrases: Monitoring system, wireless sensor network, high-frequency sampling, rock collapse forecasting.

ACM Reference Format:
Alippi, C., Camplani, R., Galperti, C., Marullo, A., Roveri, M., 2012. A high frequency sampling monitoring system for environmental and structural applications. Part A: The hardware architecture ACM Trans. Sensor Netw. V, N, Article A (January YYYY), 31 pages.
DOI = 10.1145/0000000.0000000 http://doi.acm.org/10.1145/0000000.0000000

1. INTRODUCTION

Challenging environmental and structural monitoring applications, e.g., those related to rock collapse forecasting and structural health assessment, require high sampling rates to detect asynchronous events or events characterized by high frequency components. Quite often, the requested sampling rate is a few kHz, a rate introducing technological challenges whenever low energy consumption, remoteness of the deployment, distributed data synchronization, power availability and large bandwidth constraints are also requested.

The first monitoring systems for medium to high sampling rates were based on centralised solutions [Boller et al. 2009] [Farrar and Worden 2007] with sensors directly stemming in a star topology from the data acquisition board. Such a configuration al-

This article extends the work published in the Proceedings of the IEEE 7th International Conference on Mobile Adhoc and Sensor Systems (MASS), 2010.
The research activity is partly funded by the INTERREG EU project M.I.A.R.I.A. (An adaptive hydrogeological monitoring supporting the alpine integrated risk plan) Italy-Switzerland action 2007-2013, and the KIOS Cyprus-funded project.
Authors addresses: C. Alippi, R. Camplani, C. Galperti, A. Marullo, M. Roveri, Dipartimento di Elettronica e Informazione, Politecnico di Milano, Italy. Email: alippi, camplani, galperti, marullo, roveri@elet.polimi.it

DOI 10.1145/0000000.0000000 http://doi.acm.org/10.1145/0000000.0000000

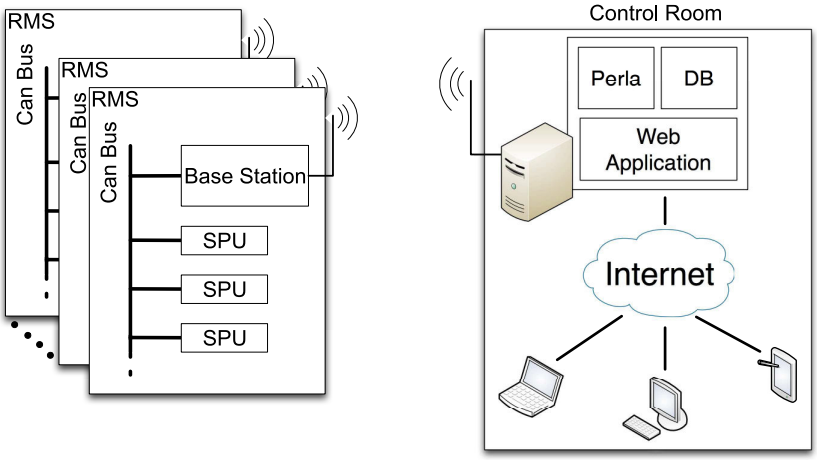

Fig. 1. The high-level architecture of the proposed hybrid monitoring system

lows the monitoring system to have a high sampling rate and data synchronism among units. Unfortunately, the peer-to-peer wired solution limits the number of probes and the deployment area covered. The length of the cable increases signal attenuation, limits its communication bandwidth and requires a long length of cables. More flexibility can be obtained by considering wireless solutions at the cost of higher energy consumption.

Herein, we propose a hybrid wireless-wired solution where advantages of wired and wireless technologies are combined to suitably address applications requiring high sampling rates. The systems approach depicted in Figure 1 presents a WSN structure where each node is a hybrid remote monitoring system. Sensing units are connected through a fieldbus and controlled by a unit exposing a wireless communication capability (base station). The base station provides energy to connected units, a local high communication bandwidth, strict time synchronisation and a remote wireless communication channel to deliver data within a mesh network configuration.

The main novel contributions of the proposed system can be summarised as:

— presentation of systems design where WSN units are the coordinators of a fieldbus-based wired network of sensors and actuators;
— a unique design for a distributed embedded system where units consume low-power (about 300mW at the 2kHz sampling rate);
— design of hardware supporting advanced hierarchical energy management policies and up-to-date energy harvesting mechanisms for low-power photovoltaic cells operating in a non-stationary environment;
— introduction of fault robustness mechanisms at the unit level;
— possibility to send commands to the remote system to change the operational mode of the electronics.

This article extends a preliminary version of the work published in [Alippi et al. 2010]; the technical material will be presented in two companion papers. The first paper, mainly devoted to hardware and architectural aspects, addresses all issues related to the hardware architecture, the designed embedded system, the fieldbus and the energy harvesting mechanism; the second manuscript targets at software aspects including data communication protocols, unit management, remote web software interface, control room design and data interpretation. The companion paper can be found

in [Alippi et al. 2012]; this paper addresses the hardware aspects and is structured as follows. Section 2 critically analyses and contrasts available monitoring systems for high-frequency sampling found in the literature. Section 3 introduces the application requirements and the architecture of the hierarchical wireless-hybrid monitoring system proposed. Section 4 presents the sensor and processing units; base station design and CANbus aspects are detailed in Section 5. Section 6 focuses on the system energetic design. Finally, Section 7 describes the system applied to a real-world deployment, specifically designed to solve a rock collapse forecasting application.

2. STATE OF THE ART

There are several monitoring systems dealing with very high sampling rates, mostly associated with particle physics experiments or industrial monitoring; as an example, the interested reader can refer to [Dell'Acqua et al. 1993] where a read-out system for high energy physics is presented, or [Gungor and Hancke 2009; Ramamurthy et al. 2007] where high frequency sampling is used to detect faults and design preventive maintenance activities. Interestingly, a high-frequency distributed measurement system for industrial monitoring purposes is described in [Schmid et al. 2010]; herein, the goal is to detect changes in the vibrational pattern of machineries to predict the need for maintenance.

High frequency sampling for distributed monitoring systems has been primarily considered in environmental monitoring applications, e.g., those addressing landslides, unstable cliffs, rock faces and volcanic eruptions. More specifically, [Werner-Allen et al. 2006] proposed a wireless system for monitoring volcanic eruptions. Therein, 16 sensor nodes continuously sample seismic (single-axis and tri-axial seismometers) and acoustic data (through a unidirectional microphone) at 100 Hz. The system adopts the Flooding Time Synchronization Protocol [Maróti et al. 2004] to keep units synchronised. Unfortunately, the absence of energy harvesting mechanisms limited the operational lifetime of the network to 19 days. [Glaser 2005] proposed a monitoring system constisting of down-hole seismographic arrays. Each array comprises a number of independent sensing units (dispersed in the borehole) linked with a RS-485 shared bus to a local gateway. Each unit (whose cost is approximately $6000) mounts a 16bit microprocessor fitted with a tri-axial MEMS accelerometer, tilt sensor, magnetometer and pore pressure sensor. Data coming from the accelerometer, sampled at 50 Hz, measure the seismic wave propagation, precious information for building up ground-motion predictions. The Linux-based local gateway is remotely connected to the Internet by means of a dedicated radio link. Authors claim to be able to guarantee sampling rates up to 250Hz. This constraint is imposed by the TinyOS operating system which, by adopting a run-to-completion scheduling mode, cannot guarantee any time execution deadline for the sampling and processing phases. The power consumption aspect is critical here since each unit consumes about 400 mW (probably since the operational setup is set to 50Hz) and the local gateway is always active (no duty-cycle) to provide the synchronisation clock tick to all bus-connected sensing units.

[Ingelrest et al. 2010] presents an interesting hardware/software architecture for environmental monitoring systems. Several deployments are presented and discussed (including the monitoring of a glacier and a bridge) but the sampling rate is low since the designed framework was designed for hydrological and micro-meteorological monitoring applications.

Different application scenarios for high-frequency data monitoring are presented in [Eisenman et al. 2009] and [Hu et al. 2009]. [Eisenman et al. 2009] suggests a mobile networked system for bicyclists aiming at measuring the cyclist performance and environmental data. The hardware platform is Moteiv Tmote Invent [Moteiv 2007], fitted with a two axis accelerometer (sampled at 115Hz) to measure the angle and

the lateral tilt of the bicycle. The prototyping units are powered by off-line rechargeable batteries without any energy harvesting mechanisms. [Hu et al. 2009] presents a WSN-based distributed system for monitoring the population of native frogs and invasive cane toad in northern Australia through an automatic recognition of the animal vocalization. Acoustic signals require high sampling rates (up to 10kHz) and complex processing. The proposed system is organized in two layers: low-power Mica2 motes (7.7MHz Atmega processor, 512Kb flash memory) [CrossBow 2009] acquire acoustic signals through microphones, locally process and transmit them to a Stargate board (400MHz Intel PXA processor, 64Mb RAM, 32Mb flash memory) for further processing and signal classification. Since the mote lifetime is approximately 4 days, authors proposed the use of rechargeable batteries and solar panels but details about the envisaged technological solutions have not been provided.

Structural Health Monitoring (SHM) applications [Farrar et al. 2011] [Boller et al. 2009] [Grattan et al. 2009] require data to assess the structural properties of civil and aerospace infrastructures. Most of the time, accelerometers are embedded in the sensor platform to identify possible changes at the structural level (e.g., by evaluating changes in the natural resonance frequency [Farrar and Worden 2007]). The sampling rates of these systems generally range from 50Hz to 1kHz.

Traditional SHM systems are based on a centralised acquisition board which periodically samples data from wire-connected probes. This solution guarantees synchronous samples among different acquisition channels. However, the reduced length of the probe cables and the limited number of signal acquisition ports limit the size of the deployment area.

To overcome these limitations, [Caicedo et al. 2002; Engel et al. 2004] introduced a radio-based probe in which the signals acquired are directly sent to a central acquisition board by means of a radio module and no local processing is performed. [Lynch et al. 2004; Lynch et al. 2003] introduced the concept of smart sensors [Akyildiz et al. 2002] in the SHM field. The sensing units proposed process locally acquired data (i.e., through a FFT transform) and transmit remotely only the outcome of the computation (i.e., the relevant FFT coefficients); synchronisation aspects and energy harvesting mechanisms are not considered. [Lim and Shoureshi 2003; 2006] suggested a monitoring system for structural integrity of power lines based on the electromagnetic-acoustic transducer (EMAT) sensor [Johnson et al. 1994]. Sensing units observe the propagation of electromagnetic pulses through the cable to detect potential structural damages (e.g., broken strands and/or corrosion). The signals acquired are locally filtered and classified by means of a neural network to identify the type of the damage; sensing units only act as data-loggers, since no transmission mechanism is provided. [Basharat et al. 2005] proposed a heterogeneous system consisting of a WSN and a set of wired cameras. The WSN nodes acquire signals from 2 MEMS accelerometers: the first one, which has a reduced measurement range, aims at detecting the natural oscillations of the structure; the latter, characterised by a larger measurement range, is used to detect anomalous shocks. The events registered by both MEMSs are then forwarded to the gateway for further processing (the gateway switches the cameras on only if an event is detected). [Kim et al. 2007] suggested a wireless sensors network to monitor the Golden Gate bridge. The peculiarity of this system is the in-line architecture of the involved WSN nodes. A command sent from the control room activates the acquisition phase for all nodes, which store up to 20 minutes of measurements to a flash memory. When the registration ends, nodes transmit data to the gateway. Curiously enough, this phase, which relies on a 46-hop protocol, requires 12 hours to reliably convey all the data acquired to the base station. A similar approach is presented in [Rice and Spencer Jr 2009; 2008].

A wireless sensor network for structural health monitoring is presented in [Paek et al. 2005]. A set of Mica2 motes acquires tri-axial accelerometer measurements at 50Hz and transmits them to a sink by exploiting a multi-hop architecture of the network. Details about energy harvesting or energy management mechanisms are not provided. Interestingly, [Paek et al. 2010] re-implemented the system suggested in [Paek et al. 2005] through the proposed Tenet architecture. This novel multi-tiered architecture improves the scalability and flexibility of the system and allows for the remote updating of application parameters (e.g., the sampling frequency).

A critical comparison of the solutions presented above is summarised in Table I and clearly shows that synchronisation, remote reconfigurability, and effective energy harvesting still remain open issues for high sampling rate monitoring systems. Unfortunately, these application requirements are not negligible in the design of effective and credible WSNs able to operate in harsh environments while guaranteeing a long lifetime of the network at those challenging sampling frequencies. In particular, synchronisation is essential for the analysis of high frequency events since even a minimal time skew might introduce large errors e.g., in the detection and localisation of a damage. The remote reconfigurability allows for fine tuning of the system after its deployment. This feature, which is essential for scenarios characterised by a sparse knowledge of the phenomenon under investigation, allows the designer to tailor the solution parameters (e.g., filter taps and thresholds) to the application needs on-line. At the same time, it allows the system to track changes in the environment, e.g., due to non-stationarity phenomena by adapting offsets, gains and other parameters ruling the system-environment interaction. Finally, energy harvesting mechanisms are mandatory for long life-time deployments since the battery would otherwise last only a few days, given the high sampling rates. It is worth noting that effective and efficient mechanisms which are able to maximise the energy harvested from solar panels working in non-optimal conditions (e.g., presence of clouds and rain, dust and water affecting the solar cell) should be considered in real-world applications.

3. APPLICATION REQUIREMENTS AND SYSTEM DESIGN

The application requirements of strict synchronisation among units, remote reconfigurability and energy sustainability pose a challenging design issue for the monitoring infrastructure and the embedded electronics, which need to provide high performance (high communication throughput and sampling rate, strict real-time decision making ability and application code reconfigurability to track environmental changes) within an energy hungry application in an environment of reduced energy availability. The trade-off between performance and constraints satisfaction was reached by considering the hybrid wired-wireless monitoring system presented in Figure 1.

The monitoring system consists of one or more *Remote Monitoring Sub-systems* (RMSs) acquiring data from the environment and a control room whose goal is to retrieve measurement data from the RMSs for storage and further processing. Since each RMS monitors the environment independently of the others (units aimed at monitoring the same environmental niche are grouped in the RMS), we will describe a single RMS. Note that the base station of an RMS provides the wireless mechanism for building up a WSN, having each node as a terminal point of the wired-wireless network.

A generic RMS consists of the *base station* (BS) connecting a cluster of *sensing and processing units* (SPU) by means of a field bus (e.g., CAN bus). SPUs acquire and *locally process* the gathered data (e.g., MEMS, geophones, temperature, strain gauge sensors) and provide a possible actuation action. The BS collects data coming from the SPUs and transmits them remotely to the Control Room (e.g., by means of a WiFi, UMTS or GPRS link).

Table I. Comparison table

	HW platform	*Sensors*	*Sampling Frequency*	*Synchroniz.*	*Remote Config.*	*Energy Harvesting*	*Local Processing*
Seismographic arrays [Glaser 2005]	Custom unit	tri-axial MEMS	50Hz	Yes	No	Yes	Yes
Volcanic eruptions [Werner-Allen et al. 2006]	Moteiv Tmote Sky	single/triaxial seismometers, microphone	100Hz	Yes	No	No	Yes
BikeNet [Eisenman et al. 2009]	Moteiv Tmote Invent	Two axis accelerometer, magnetic sensors, GPS	115Hz	Yes	No	Yes/No	Yes
Cane toad monitoring [Hu et al. 2009]	Mica2, Stargate	Microphone	10kHz	Yes	No	No	Yes
SHM [Caicedo et al. 2002]	Analog board	Piezoeletric MEMS	200Hz	No	No	No	No
SHM [Engel et al. 2004]	Custom	Tri-axial MEMS	100-650Hz	No	No	No	No
SHM [Lynch et al. 2004]	Custom board with 8-bit AVR, 32-bit PowerPc	Dual-axial MEMS	976Hz	No	No	No	Yes
SHM [Basharat et al. 2005]	MicaZ	Tri-axial MEMS, temperature, video cameras	150Hz	Yes	No	No	Yes
SHM [Kim et al. 2007]	MicaZ, custom acquisitiono board	Dual-axial MEMS	1kHz	Yes	No	No	Yes
SHM [Rice and Spencer Jr 2008]	Imote2, custom acquisition board	Tri-axial MEMS, temperature	50-280Hz	Yes	No	No	Yes
SHM [Paek et al. 2005].	Mica2	Vibration Card	50-160Hz	Yes	No	No	Yes
SHM [Paek et al. 2010]	Mica2/MicaZ	Vibration Card	50-160Hz	Yes	Yes	No	Yes

The remote control room stores and processes the data acquired (e.g., for filtering, pattern recognition, remote decision making). At the same time, the control room allows a human operator, or the system itself, to remotely change the parameters of the RMS through a simple web application by relying on decision making algorithms.

The BS provides both synchronisation among units and power supply to SPUs; at the same time, a CAN bus solution guarantees a maximum skew among units below 0.5ms (details can be found in the companion paper [Alippi et al. 2012]). This hybrid architecture allows us to centralise the energy harvesting mechanisms at the BS level, which is endowed with solar panels and deployed in a safer, easily accessible, area (whereas SPUs generally are not in a safe area).

Design Rationale

The need to jointly address two opposite goals, such as high sampling acquisition rates and long system lifetime, led us to consider a novel hybrid system architecture. This hybrid wired-wireless solution aims at providing the advantages of the wired systems in terms of energy efficiency and high synchronisation among the acquisition units while maintaining the scalability and flexibility typical of wireless solutions.

In addition, such an architecture allowed us to design and develop SPUs without batteries and solar panels since the energy harvesting mechanisms are centralised at the BS. SPUs can thus be simpler, cheaper and smaller in size and weight. Deployed units are required to be light and small in size since they are hung on the rock face by means of holes and fixed with an ad-hoc resin. The absence of solar panels and, in particular, of the battery allowed us to significantly reduce both the size and the weight of the SPUs (see Section 4.4).

In such critical environmental conditions, the presence of solar panels on the SPUs would introduce two additional drawbacks. Firstly, vibrations induced by the wind on the solar panels would propagate to the SPU case, thus affecting the acquisition phase of geophones and accelerometers (e.g., inducing false events). Secondly, the orientation of the solar panels is very difficult, whenever applicable, thus reducing the energy harvesting efficiency.

In summary, the fully wireless solution, which is in principle feasible, would have significantly increased both the complexity and the cost of the overall system as well as introduced possible bandwidth problems when bursts of events happen. Differently, a hybrid solution allows us to centralise both the energy harvester and the synchronisation issue, thus leading to a more credible and cheaper solution.

The choice of the CAN bus as fieldbus for the RMSs deserves a specific discussion. Although several well-known technological solutions are in principle available (e.g., RS485, Industrial Ethernet, ProfiBus, ControlNet), we opted for the CAN bus for two reasons. Firstly, the CAN bus is a widely accepted standard vendor free solution (e.g., ProfiBus is a Siemens's solution). For this reason, many microcontrollers and industrial PC104 boards are fitted with CAN bus interfaces. Secondly, the CAN bus provides both the physical and the MAC layers of the communication stack, whereas other fieldbuses (e.g., the RS485) do not specify or suggest any communication protocol. This allowed us to simplify the design of the communication layer among the acquisition units.

Hereinafter in the paper we detail the main components of the RMS i.e., the SPU, the Base Station and the fieldbus; details related to the software are described in the companion paper [Alippi et al. 2012].

4. SENSOR AND PROCESSING UNITS

SPUs acquire measurements from sensors, carry out local processing to extract features from sensor data and transmit them to the BS. As presented in Figure 2, electronics-wise SPUs are organised in two boards and a set of sensors, i.e., strain gauge, temperature, MEMS accelerometer, inclinometer and geophones. The SPUs are connected to the BS by means of the CANbus which provides both the energy supply and the transmission medium.

In more detail, each SPU has been designed as two vertically-stacked electronic boards, the first one carrying out processing and communication (see Section 4.1), the second one signal conditioning (see Section 4.2). The two boards are suitably tied together with connectors and screws. The vertically-stacked architecture has been designed to reduce the size.

As detailed in Section 4.3, each SPU is fitted with a tri-axial MEMS accelerometer and a temperature sensor (to be used for thermal compensation and get indications about the frost/defrost cycle). The MEMS accelerometer provides both accelerometer and inclinometer information. To provide a more detailed view of the physical phenomenon under monitoring, the SPU could be fitted with a geophone or a strain gauge. The geophone can provide information about the movements of the ground (in this case, the MEMS accelerometer only provides information about the inclination; accelerometer measurements are not acquired), while the strain gauge allows the deformation of a pre-existing fracture to be monitored.

An ad-hoc case, which is detailed in Section 4.4, has been designed and manufactured to reduce the overall unit size and dissipate thermal energy by convection, to ease the deployment phase and avoid unwanted mechanical resonance of the case falling in the 1kHz bandwidth. The cost of an SPU (boards, case and sensors) in this

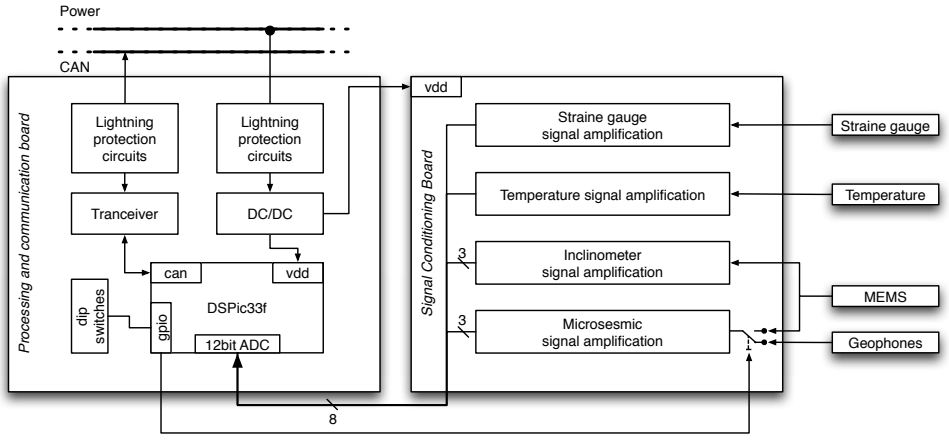

Fig. 2. The architecture of the SPU.

low volume version is around 1000 euros. The cost would be significantly reduced with a large scale production.

4.1. The processing and communication board

The processing and communication board (see Figure 3a and 3b) basically consists of five main parts: a microcontroller, CAN transceiver, lighting protection circuits, dip switches and DC/DC power regulator circuit.

Among the wide range of microcontrollers available on the market we opted for a digital signal processor (DSP) since it provides the hardware capability required to carry out an efficient mathematical processing of a data stream (e.g., digital filtering and FFT).

In particular, we selected the ultra-low power DSP Microchip DSPic33F operating at 40MHz and providing a simple 16-bit microcontroller architecture as well as an up to date two-bus DSP architecture with a 40 bit multiply and accumulate unit and two separate hardware address generators. The microcontroller fetches code for execution from the internal flash memory, uses an internal SRAM memory for data storage and provides on-chip peripheral devices for external interfaces (such as *CAN*).

Based on our expertise, this ultra-low power DSP guarantees the best trade-off between performance and power consumption. Off-the-shelf 16bit microcontrollers (e.g., PIC18, MSP430, Cortex M0) do not provide DSP functionalities in hardware (which must be executed in software, thus increasing the power consumption of the SPUs). On the contrary, standard 32bit DSPs (e.g., Sharc by Analog Devices, the Texas Instrument C6000 or the Cortex-based STM32F4) provide higher computational performance at the expenses of an unacceptable power consumption in our applications (e.g., the power consumption of these standard 32bit DPSs ranges between 500mW and 2.5W in a fully active mode, while the envisaged 16bit DSP only consumes 300mW in the same mode).

The basic tasks carried out by the DSPic33F are:

(1) Sampling sensor signals coming from the conditioning circuit;
(2) Processing the digital data stream at 2k samples per second (for all connected sensors requiring a high sampling rate);
(3) Storing processed data to the internal SRAM memory.

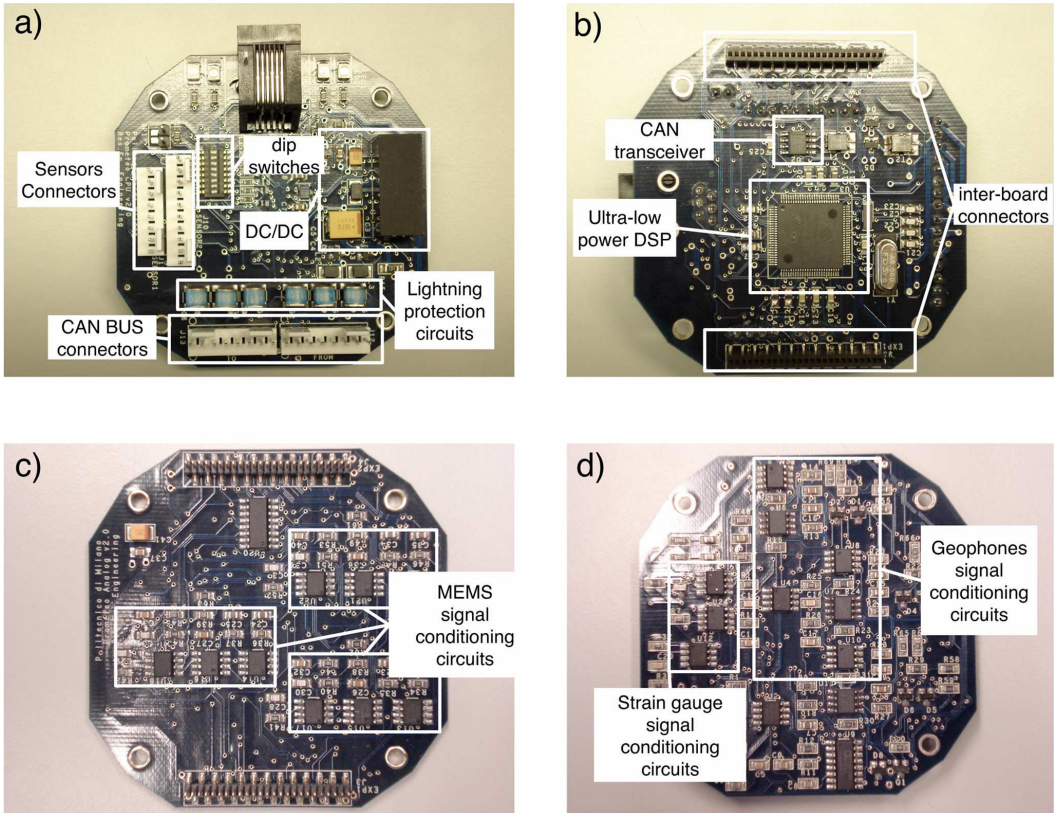

Fig. 3. The boards composing the SPUs: a) Processing and communication board [upper side]; b) Processing and communication board [lower side]; c) Signal conditioning board [upper side]; c) Signal conditioning board [lower side].

The CAN transceiver is a circuit controlling the connection and data propagation along the CAN bus. As such, it represents the physical layer of the CAN stack; the MAC and the network layers are handled by the microcontroller. We chose the Texas Instruments ISO1050 CAN transceiver since it provides the opto-isolation between the processing and communication board and the CAN bus (thus guaranteeing robustness to overvoltage up to 4000V).

The lighting protection circuits aim at preventing the effects of lightings (in terms of overvoltage and overcurrent) that could fall in the neighbourhood of the system (the risk of lighting is high for an environmental monitoring application). Figure 4a and Figure 4b show the protection circuit for the power lines and the CAN bus lines, respectively. These circuits, which are separately applied to the power lines and the CAN bus since the latter is opto-isolated, share the same mechanism: the transient voltage suppressors (i.e., G1 to G6) aim at preventing overvoltage peaks, while the choke inductors (i.e., L1 to L6) handle overcurrent peaks. It is noted that we inserted a transient voltage suppressor for each couple of wires to be able to avoid overvoltages among VDD, circuit ground and case ground in the power lines and among the differential CANH, CANL lines and case ground in the CAN bus line. Since the CAN bus is a differential line, the choke inductors L3 to L6 are coupled to reduce noise. In addition, we introduced the protection electrostatic dischargers (PESD1 to PESD4) to protect circuits from electrostatic discharges induced, for example, by human operators touch-

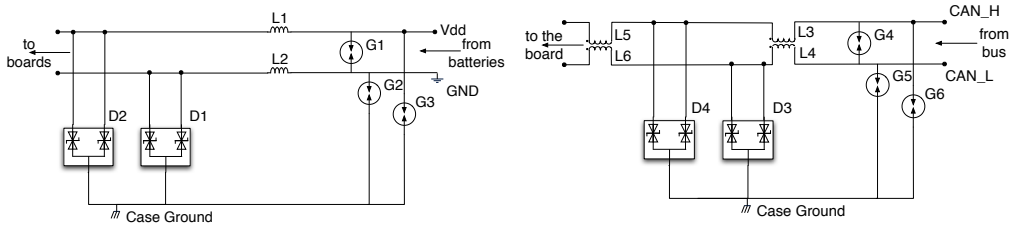

(a) Protection for power lines (b) Protection for CAN bus lines

Fig. 4. Lightning current/surge arrester

ing the circuits. The decision to design an ad-hoc lighting protection circuit (rather than considering off-the-shelf lighting protection circuits) is justified by the possibility of integrating the circuit directly on the board (as depicted in Figure 2).

The dip switches circuit aims at storing the in-field configuration of the node (i.e., the Node ID and CAN bus baud rate). The switches are manually fixed by designers and read, during the initialisation phase to configure the node, as detailed in Section 4 of the companion paper. The dip switches circuit we chose is the Multicomp MCDHN-08-V with 8 switches and 1.27 pitch; other dip switch circuits with the same electronic characteristics could be considered as well.

Finally, the DC/DC power regulator circuit adapts the 12V provided through the power supply line to the 3.3V requested by the processing and communication and the signal conditioning boards. We adopted the TRACO TMR 1210, which operates in the range of 9-18VDC, with a conversion efficiency of 70% for an output voltage of 3.3V.

The advantage of a DC/DC regulator present in the processing and communication board of each SPU (instead of adopting just a centralised DC/DC at the BS) is twofold. Firstly, the galvanic isolation provided by the TRACO allows the ground of the cable from the one of the SPU boards to be decoupled, thus increasing the overvoltage protection on the cable. In particular, the selected TRACO guarantees the management of overvoltage up to 1000VDC. Secondly, the DC/DC at each SPU guarantees a stable reference voltage for both the processing and communication board and the signal conditioning one. In particular, variations in the reference voltage of the signal conditioning board could induce errors in the analogue-to-digital conversion, thus affecting the acquired measurements. Moreover, any glitches in the supply voltage of the microcontroller could generate spontaneous, unwanted reset actions.

4.2. The signal conditioning board

The *signal conditioning board* (see Figure 3c and 3d) contains the signal conditioning circuits for the attached sensors. This board, together with the application code executed on the SPUs, is application-specific, whereas the processing and communication board (presented in the previous subsection) can manage a large class of applications being able to deal with both low and high bandwidth sensors.

As presented above and detailed in Section 4.3, the set of considered sensors encompasses both low-bandwidth sensors, e.g., strain gauges, inclinometer and temperature sensors, and high-bandwidth sensors, such as MEMS accelerometers and geophones.

Accordingly, the signal conditioning board hosts 6 conditioning channels for the MEMS sensor (3 for the tri-axial acceleration AC component and 3 for the tri-axial acceleration DC component), 3 channels for the geophones and one channel for the strain gauge sensor.

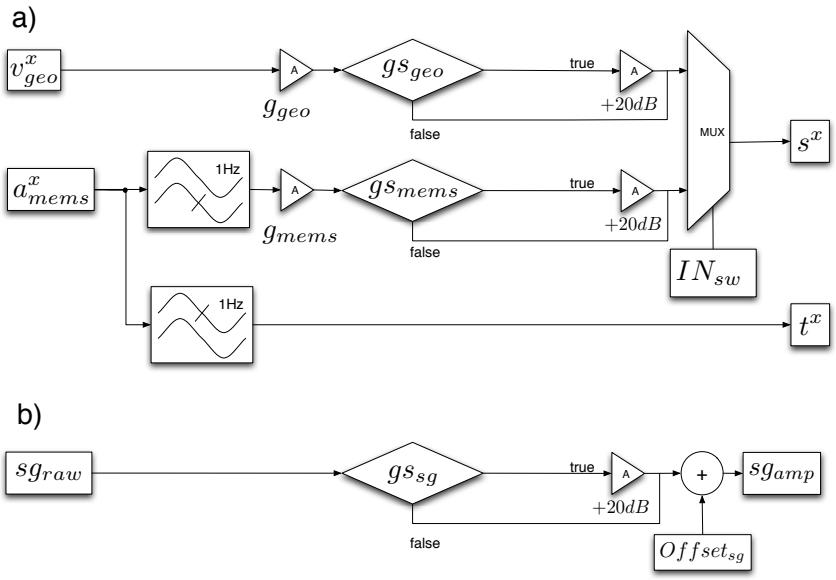

Fig. 5. Block scheme of the Signal conditioning board: a) Conditioning circuit for the x component of the geophone and the MEMS accelerometer; b) Conditioning circuit for the strain gauge.

Figure 5 details the block scheme of the signal conditioning board. In particular, Figure 5a presents the signal conditioning circuit for the x channel of a geophone or MEMS accelerometer (channel y and z are omitted for figure readability), while Figure 5b shows the signal conditioning circuit for the strain gauge. Geophone signals v^x_{geo} are initially magnified by an amplification parameter of gain g_{geo}. Then, if necessary, signals can be further magnified by $+20dB$ simply by setting the value of gs_{geo} to 1 (logical TRUE).

Accelerometer signals a^x_{mems} are initially filtered by means of analogue low-pass and high-pass filters with cut-off frequency at 1 Hz to separate the static component of the signal t^x (representing the projection of the gravitation acceleration $\vec{g}$ vector along the xth component) and the dynamic component (representing the acceleration along the axes). The latter is then amplified by g_{mems} with a value of up to $+20dB$ (when gs_{mems} is equal to 1). The input IN_{sw} to the multiplexer specifies whether the geophone or the accelerometer signals has to be considered; this input is set at the software level.

Strain gauge signal sg_{raw} is amplified by $+20dB$ if gs_{sg} is 1 and an offset $Offset_{sg}$ is added for compensation. In particular, the signal conditioning circuit for strain gauge exposes a magnification ability which enables the remote operator to zoom a particular part of the measuring range. The zooming factor has been fixed to 5, while the offset on the measuring range can be configured remotely.

The parameters of these circuits, summarised in Table II, have been designed to be modified at run-time, thanks to digital potentiometers and digital switches (each SPU has 24 tunable parameters). In particular, the digital potentiometers, connected to the DSPic through the SPI bus, adjust the impedance between the different operational amplifiers comprising the analogue filters and amplifiers on the sensor board, while the digital switches, commanded through simple GPIO lines, alternate different sets of capacitors and resistors on the same circuits. This parametric-computation approach is a fundamental tool for designing robust adaptive monitoring systems able to adapt to changes in the environment.

Table II. SPU hardware parameters (dafault values are in bold)

Parameter Name	*Function*	*Range*
g_{mems}	MEMS signals amplifier gains (3 channels)	$(0 - 40dB)$
gs_{mems}	MEMS gain switch (add $20dB$ to M_G)	$\{true, \mathbf{false}\}$
g_{geo}	Geophone signals amplifier gains (3 channels)	$(8 - 60dB)$
gs_{geo}	Geophone gain switch (add $20dB$ to G_G)	$\{true, \mathbf{false}\}$
$Offset_{sg}$	Strain gauge zoom offset	$(0 - 255)$
gs_{sg}	Strain gauge zoom enable	$\{true, \mathbf{false}\}$
IN_{sw}	Input selection switch	$\{\mathbf{MEMS} = 1, Geophone = 0\}$

4.3. Sensors

MEMS accelerometers and geophones are the sensors to be used for acquiring micro-acoustic signals in environmental or structural monitoring applications. To satisfy this requirement we considered a 2kHz sampling rate, hence MEMS accelerometers and geophones are able to detect signals up to 1kHz in bandwidth. Such a bandwidth allows the SPUs to acquire signals in the band typical of both SHM applications (50Hz to 1kHz) and high sampling-frequency environmental applications (1Hz to 1kHz). In addition to a tri-axial accelerometer or geophone, each SPU mounts traditional sensors such as a strain gauge, an inclinometer and a temperature sensor.

The MEMS accelerometer used is the low power tri-axial ST LIS3L02AL developed by ST Microelectronics (range $\pm 2g$, resolution 0.5mg). We opted for an analogue accelerometer since off-the-shelf digital accelerometers provide lower sampling frequencies (sampling rates up to 250Hz). In addition, in our opinion, the selected accelerometer guarantees the best trade-off between performance and cost, while maintaining very small sizes (5mm $\times$ 5mm). The three channels are sampled at 2kHz with a 12bit resolution. Similar to other MEMS accelerometers, the continuous component of the acquired acceleration measurements represents the projection of vector $\vec{g}$ on the axes of the MEMS, thus providing information about the inclination of the sensor.

The selected geophone is manufactured by Solgeo [Solgeo 2012] and includes a tern GeoSpace GS-20DH geophones to support three-dimensional sensing. These geophones are passive and guarantee a bandwidth of up to 400Hz. Having said that, our electronics is able to host a large variety of geophones.

The temperature sensor used is the Microchip TC1047A. The temperature ranges from -40 °C to +125 °C with an accuracy of 0.5 °C and is sampled with a 12bit resolution. Other temperature sensors providing the same electrical characteristics (supply voltage 3.3V, sensor output voltage 1.75V) would fit well with the electronics.

Among the wide range of strain gauges (with current output 4-20mA) available on the market, we focused on the SISGEO 0D313SA1000 [Sisgeo 2012], for its sensitivity (operating range 300mm$\pm$50mm, resolution 0.01mm, repeatability $< 0.3\%$ of the full scale). Also the strain gauge is sampled at 12 bits.

The sensors considered are summarised in Table III. It is worth noting that we cannot envisage (and it would be a nuisance) a continuous transmission of the acquired data to the control room since microacoustic emissions are asynchronous burst-type events and the required data bandwidth is high (12bits $\cdot$ 3 channels $\cdot$ 2k samples). Moreover given the low expected number of events (sparse data over time) e.g., 0-10 events per week, triggering mechanisms based on noise-to-signal ratio can be used at SPU level to detect the presence of micro-acoustic bursts [Alippi et al. 2007] and the data is sent to the base station only when a possible event is detected.

4.4. The case

In monitoring systems designed to work in real-life (possibly harsh) environments, the correct design of the unit case is important as the correct design of the hardware and

Table III. SPU Sensors

Type	*Sensor model*	*Range*	*Resolution*	*Accuracy*
MEMS	ST LIS3L02AL	$\pm 2g$	$0.5mg$	N.A.
Geophone	Three-dimensional board of GeoSpace GS-20DH geophones	28-400Hz	na	na
Strain gauge	SISGEO 0D313SA1000	$300mm \pm 50mm$	$0.01mm$	$< 0.3\%FS$
Temperature	Microchip TC1047A	-40°C to $+125$°C	N.A.	± 0.5

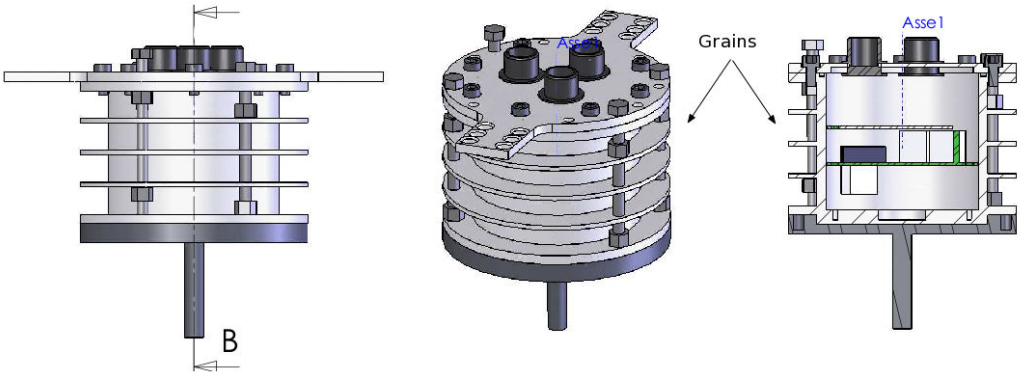

Fig. 6. The design sketch of the case.

software. Though several off-the-shelf cases or switch gears are available, we had to design an ad-hoc case due to the peculiar application scenarios we are considering. In fact, traditional cases for WSN units are not designed to be hung from a rock face and cannot guarantee not to interfere with the signal.

Our unit case has been designed to be light and small in size. The final output is presented in Figure 6 where the cylinder has a 120mm diameter and 100mm height. The considered material is aluminium: easy to produce, lighter than steel and barely attenuates incoming microacoustic emissions. Moreover, the ability of aluminium to conduct heat allows the case to dissipate the internal thermal energy by convection through the dissipating annular wings provided in the box case.

A prototype of the case was initially made and its performance tested under vibrations by means of a shaker (see Figure 8(a) and 8(b)). Unfortunately, the first prototype was introducing a resonance at around 700Hz and therefore, interfering in the bandwidth of the signal.

We then modified the case by including grains in the upper part of the case to reduce vibrations (these grains are highlighted in Figure 6). This allowed us to remove the resonance parasitic effect (as presented in Figure 8(c),8(d)).

It is noted that, as presented in Figure 7, the case has been designed in two main components, i.e., the chassis and its support, to ease the deployment phase and maintenance. Only the support is permanently fixed to the rock face (or the monitoring structure) by means of holes and an ad-hoc resin. On the contrary, the chassis is anchored to the support by means of screws. This solution simplifies maintenance; if a unit fails, we simply replace it with a new one.

5. THE BASE STATION AND THE CAN FIELD-BUS

The base station (BS) plays a crucial role in the hybrid wireless-wired architecture since it powers the units, coordinates the communication activity among SPUs and serves as a gateway between the local system and the control room. Referring to Fig-

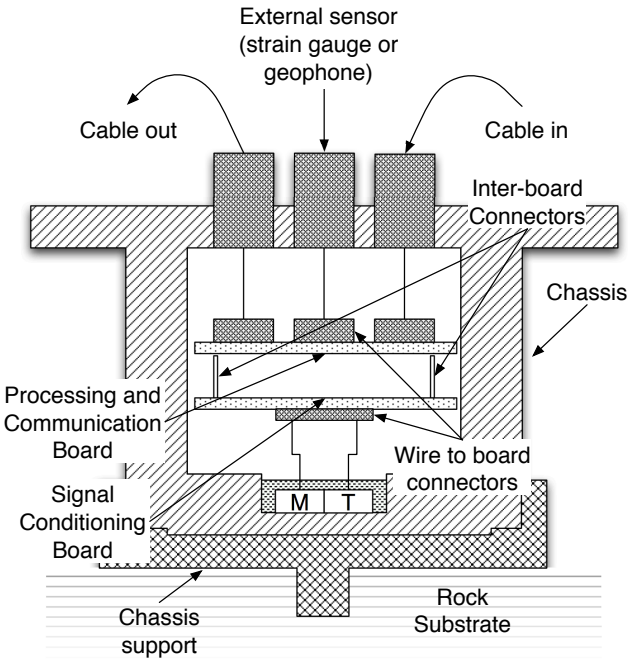

Fig. 7. A section of the case.

ure 1, the BS acts as the master of the fieldbus by collecting the data acquired and status information (e.g., uptime, software version currently installed) from the SPUs and forwards them to the control room through the remote wireless channel. At the same time, it provides mechanisms for time synchronisation at the SPUs level and dispatches commands back to the units. In its energy harvesting capacity, the BS acquires energy by means of photovoltaic cells based on a maximum power point tracker (MPPT) circuit and stores it into batteries (e.g., lead-acid batteries).

Figure 9 shows a picture of the base station whose block diagram representation is given in Figure 10.

In particular, the BS comprises

(1) the *main board*, which mounts the main microprocessor executing the application tasks;
(2) the *energy harvesting board*. It contains the MPPT and reports the status of the energy harvester to the main board;
(3) the *shut-down/wake-up board*, which allows the main board to undergo duty cycling mechanisms;
(4) the *energy management board*, whose task is to enforce power management policies depending on the battery voltage;
(5) the *radio module*, either consisting of a radio link (e.g., a 5GHz WiFi) or an UMTS modem.

It is noted that it is not required for the BS to be deployed on the rock face or on a structure close to the units. In fact, thanks to the fieldbus, it can be placed in a safe and easily reachable area. The BS is contained in the off-the-shelf Gewiss GW44811 switch gear hung from a pole; the box size is 396 x 474 x 160mm.

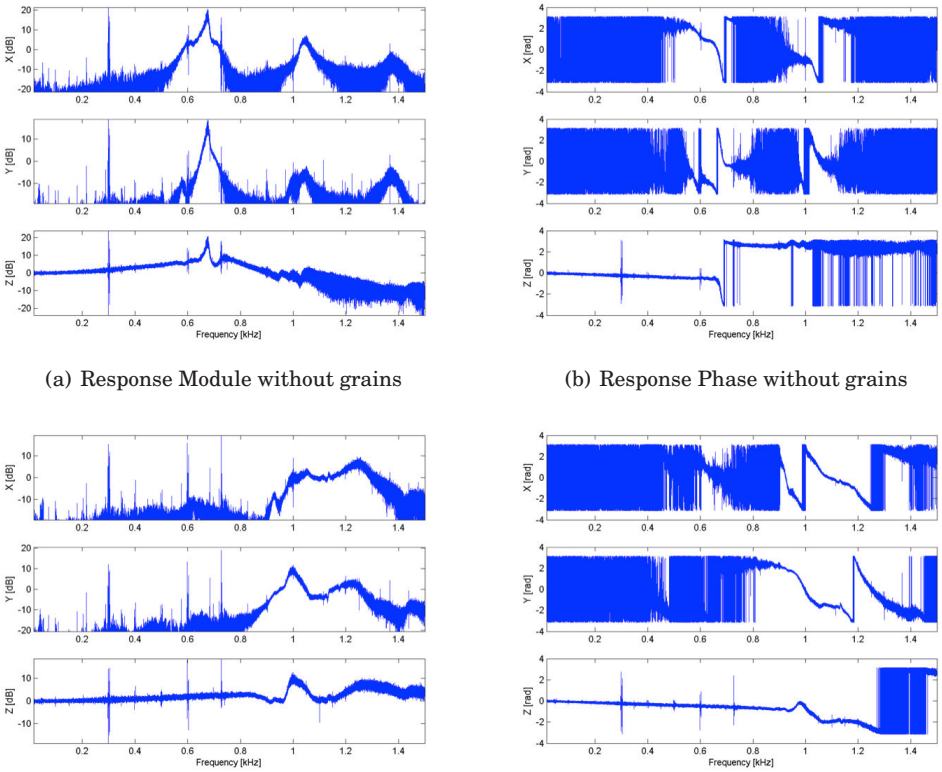

(a) Response Module without grains

(b) Response Phase without grains

(c) Response Module with grains

(d) Response Phase with grains

Fig. 8. The Bode diagram (module and phase) of the case prototype without and with grains.

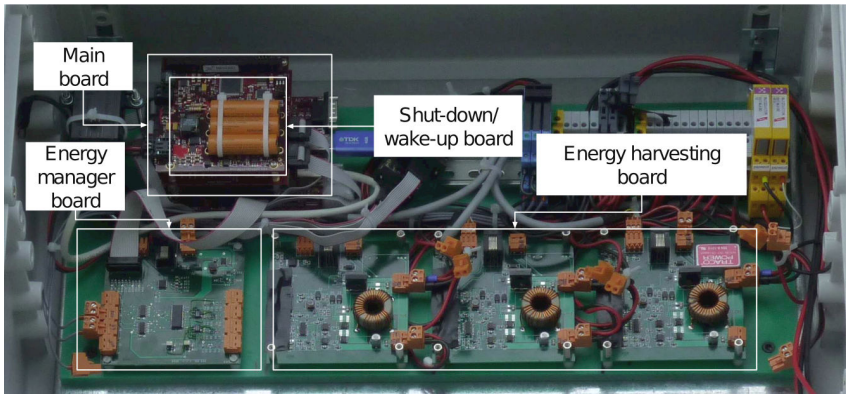

Fig. 9. A picture of the base station showing the main modules. The radio module is not here visible as integrated in the antenna (which is outside the case).

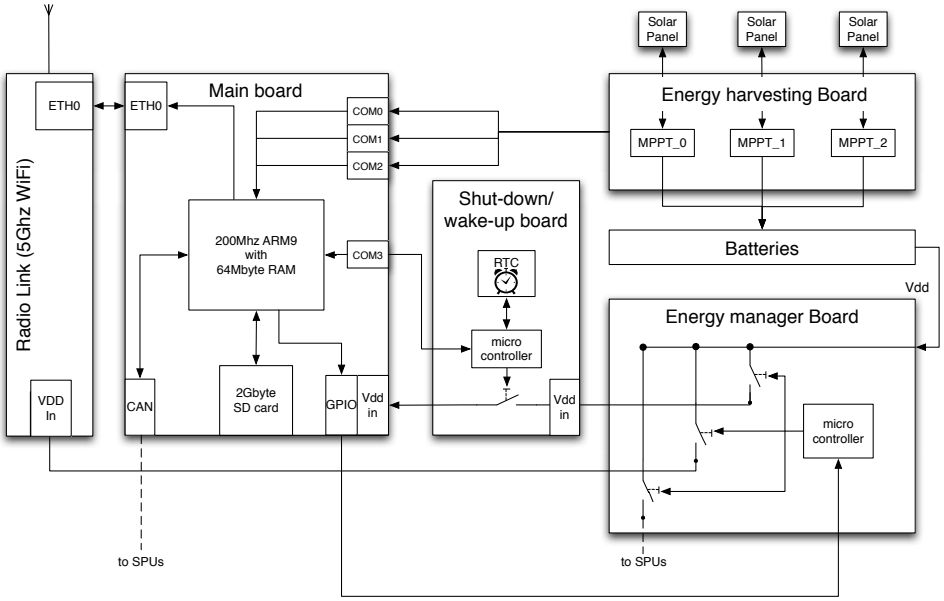

Fig. 10. The architecture of the base station

Similarly to SPUs, the main board is fitted with the lighting protection circuit (refer to Section 4) shielding both power and CAN bus lines. In addition, the BS is fitted with rechargeable batteries and solar panels to guarantee the system credibility energy-wise. We considered Lead-acid 12V 30Ah UNIBAT and the Lead-acid 12V 40Ah UNIBAT batteries, which share the same technology but differ in the energy charge mechanism, size and weight. The choice between these two batteries is a design issue and is related to the amount of energy required by the system. We need to use lead-acid batteries since this technology guarantees a higher life-time of the battery in terms of charge-discharge cycles. For solar panels, we considered a polycrystalline 20W nominal solar panel manufactured by RALOSS (RALOSS-SR20-36). Other solar panels providing the same technical characteristics could have been considered as well.

5.1. Main Board

The main board is also the mother-board for the whole system. Here, we opted for the PC104-based Technology System TS7260 board based on an ARM9 200MHz microprocessor and fitted with 64MByte of RAM, 14 general purpose I/O (GPIO) lines, four serial lines, a USB pen driver and an SD card reader. Moreover, the board is endowed with both a CAN and an Ethernet port to communicate with the SPUs and the radio link, respectively. The GPIO communicates with the energy manager board, while the serial ports provide the communication link with the shut-down/wake-up and the energy harvesting boards. We chose the PC104 technology since it guarantees both lower power consumptions (w.r.t. other boards based on the x86 technology) and reduced size (which in our case is an important constraint). However, other PC104-based boards with similar electronics could have been considered as well. The main board stores both the operating system (Linux) and the application code in a read-only 2GB SD card (Trascend Industrial Grade TS2GSD80I 2GB SD card) to prevent any unintentional modification of the code, while data (collected from SPUs and ready to

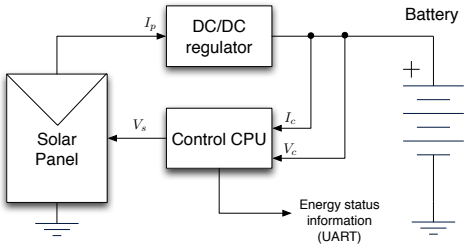

Fig. 11. The block diagram of MPPT circuits. V_s, I_p, V_c and I_c are the voltage of the solar panel, the current generated by the solar panel, the output voltage and current from the DC/DC regulator, respectively.

be transmitted to the Control Room) are stored as files to the USB pen drive (STEC Industrial Grade SLUFD2GU1U USB 2GB Flash Drive). In case of a USB pen drive fault, this solution allows the BS to inform the control room about the fault occurred. It is noted that both the SD card and the USB pen drive must be certified as industrial grade so as to work in extreme temperatures ranging between -40°C to +85°C interval.

The application code, detailed in [Alippi et al. 2012], consists of a script polling the SPUs for data acquisition, storing data to files, opening the connection with the remote control room and transmitting data. Finally, it receives commands that, suitably parsed, are dispatched back to the targeted SPU. The CAN port of the main board allows for the BS to be connected with the SPUs by means of the industrial CANbus (version 2.0b) providing both the physical and the MAC layers in hardware. The maximum bandwidth is 1Mbps for cables up to 40m and decreases with the cable length (e.g., the maximum bandwidth for a 100m long cable is 250kbps).

Although several transport layers for CANbus have been presented in the literature (e.g., see CANOpen [Lawrenz 1997]), they cannot be used in energy aware applications since the energy aspect is not tackled: being designed for industrial applications, CANOpen requires the units to be always on. The proposed transport layer designed to tackle this issue will be discussed in the companion paper [Alippi et al. 2012]. Two GPIO lines provided on the main board are particularly interesting and allow the SPUs to be switched on and off at once or enable the remote radio link. These mechanisms guarantee implementation of fine-grain energy management policies.

5.2. The energy harvesting board

As stated in [Alippi and Galperti 2008], solar panels exhibit a non-linear electrical characteristic which is a function of the solar radiation and the operational temperature and are affected by ageing, dust and efficiency degradation. These time-varying non-linear effects can make traditional (diode-based) energy harvesting mechanisms very inefficient as they require the solar panel voltage to be basically above that of the storage means.

The suggested energy harvesting board relies on a maximum power point tracker (MPPT) circuit [Alippi and Galperti 2008] which sets the voltage of the solar panel to an optimal value, maximising the power transferred. This optimisation step is carried out by continuously adapting the working point of the photovoltaic cells to the optimal value. In addition, the MPPT circuit used, presented in Figure 11, consists of two main blocks: an adaptive digital control loop and a voltage input controllable DC/DC converter stage. The first block consists of a microcontroller, whose code adaptively identifies the optimal working point for the solar cells by setting the optimal voltage V_s and maximising the extracted power. In addition, the microcontroller reports the battery voltage status to the main board through a serial port for subsequent decision making. The second block, which is implemented by means of a single-ended primary-

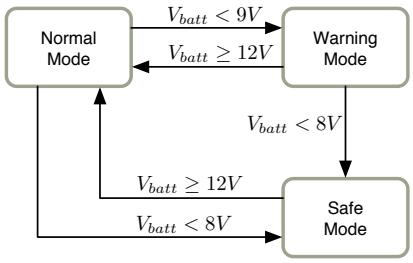

Fig. 12. Behaviour of the energy manager

inductor converter (SEPIC) circuit, aims at adapting the input (cells) voltage identified by the microcontroller of the solar panel with that of the storage battery.

The energy harvesting board presented in Figure 10 consists of three independent MPPT circuits, each one controlling a single solar panel. Nevertheless, as described in Section 7, the number of solar panels (and consequently of MPPT circuits) is application-specific and depends on the power consumption, duty-cycle of the units and expected solar radiation of the deployment area. We decided to develop an ad-hoc energy harvesting board since off-the-shelf energy harvesting boards (e.g., traditional solar charge regulators) are not tailored for small harvested energies (hence, the energy consumption of these boards is not negligible for the energy consumptions of our system). In addition, the energy harvesting board developed provides energy information about the system such as the panel voltage, generated current and battery voltage. Such information, as presented in Section 5.3, is essential for an effective energy management. The MPPT circuit has been proved to be particularly effective even in cloudy or rainy days, situations where traditional diode-based energy harvesters proved to be inefficient at low power solar radiations. In fact, the traditional diode-based solutions are not able to harvest power when the incident solar power is below 10mW, while the used MPPT circuit can operate with incident solar powers down to 2mW, a common situation in foggy, misty or rainy days [Alippi and Galperti 2008].

5.3. The energy management board

The aim of the energy management board, whose block diagram is detailed in Figure 10, prevents the battery voltage to drop below a fixed threshold (i.e., 8V). We decided to develop an ad-hoc energy management board since the battery management circuits available on the market (e.g., traditional solar charge regulators) do not provide advanced energy management policies. Our energy management board implements an advanced energy management policy as summarised in Figure 12. In particular, when the battery voltage is above 9V (*normal mode*), the system is fully operational and no policies must be undertaken. When the battery voltage is between 8V and 9V (*warning mode*), the energy management board cuts off the power supply to the SPUs and the radio module, waits till the end of the duty-cycle of the main board and shuts down. When this happens, the energy management board idles until the voltage battery is back to 12V (thanks to solar recharging) to switch back to normal mode. We introduced a safety threshold at 8V (*safe mode*) to address unpredictable cases where the main board does not complete the shut-down operation (e.g., due to software errors, kernel panic), thus further consuming the residual energy. When the battery level drops below 8V, the energy management board cuts off the power supply of the main board regardless of shut-down completion. Even in this case, the energy management board

restores the normal operational mode only when the battery voltage returns above 12V.

5.4. The shut-down/wake-up board

The shut-down/wake-up board, whose block diagram is presented in Figure 10, allows the main board to undergo duty-cycling by switching the BS off for a certain amount of time and waking it up again when needed. The board used is the off-the-shelf Technology Systems TS-BAT3, which is a PC104 board and can be easily integrated with the PC104 main board. The selection of the board was based on compatibility issues. The main board periodically prompts the shut-down/wake-up board to shut down for a certain amount of time to save energy; this action is carried out through a message sent along the serial connection to the board. As a reply, the shut-down/wake-up board activates a timer (for the amount of time requested by the main board) and activates a relay that cuts-off the power line of the main board. Then, when the timer expires, the shut-down/wake-up board re-enables the relay, thus powering the main board, which reboots. The shut-down/wake-up board consists of a low-power micro-controller, a relay, a Real Time Clock (RTC) powered by a battery button, and a serial port connected to the main board. In particular, the micro-controller remains in a deep-sleep state until it receives an interrupt on the serial port. Thereafter, it receives the messages from the main board (containing sleeping time information) and, finally, activates an RTC timer. Afterwards, the micro-controller cuts off the power of the main board by means of the relay (that switches according to a GPIO line of the micro-controller) and enters into a deep-sleep state again to further reduce energy consumption. When the timer expires, the RTC generates an interrupt which wakes up the micro-controller which then acts on the relay to restore energy back.

5.5. The radio module

The radio module provides the remote radio link by connecting the BS with the remote control room. Two main technologies, which differ by bandwidth, power consumption and coverage area, have been considered: a radio link and a 3G UMTS modem. More specifically, the 5GHz WiFi radio link guarantees a 6Mbps TCP/IP channel for distances up to 7Km, with a peak power consumption of 4W. The main drawback of this solution is the line-of-sight requested between the antennas of the RMS (directive) and that of the remote control room. The WiFi link we selected is the Fly Communications Nebula 2458. Other 5GHz WiFi links available on the market could be considered as well. On the contrary, the UMTS modem relies on the coverage of the UMTS mobile network (no line-of-sight required) at the expenses of higher power consumption (up to 18W) and a lower bandwidth (in theory up to 5.76Mbps in up-link; in practice, generally from 500kbps to 1.5Mbps). When the UMTS network is not available, the modem automatically switches to a GPRS connection (max 14.4kbps in up-link), increases the duty-cycle (see Section 7) and accordingly, power consumption. We chose the Quad-band DIGI Connect WAN 3G modem for its flexibility (thanks to its quad-band technology) and since it can be easily controlled through the Ethernet port.

6. DESIGN OF THE SYSTEM FROM THE ENERGY POINT OF VIEW

As described in Section 4 and 5, the design of both the SPUs and the BS was low power-oriented with particular attention to the choice of the components and the hardware design. In addition, for the system to operate for years in harsh working conditions, a correct design of batteries and solar panels must be carried out. An incorrect rating of the energy harvesting module for the system can led to two unpleasant effects: 1) if the system is under-rated w.r.t batteries and solar panels, the system will run out of energy frequently (with a consequent frequent loss of measurements); 2) an over-

rated system increases the complexity, size and cost of the system. The correct design of the energy harvesting and power supply modules certainly depends on the system energy consumption which is in turn a function of the power consumption of its components and duty cycle. Let's assume that one BS and N SPUs (the number of SPUs is application-dependent and defined at the design stage) are used. The power consumption (measured in laboratory tests) of the main functional elements is given in Table IV.

Table IV. Power consumption (in W) for one SPU, the BS and the long-range radio link

	P_{SPU}	P_{BS}	P_{WiFi}	P_{GPRS}
Power Consumption (W)	0.3	2.4	4	18

Let τ_{SPU}, τ_{BS}, τ_{WiFi}, τ_{GPRS} be the duty-cycles of each SPU, BS, WiFi and GPRS link, respectively (SPUs are always operational and cannot be switched off, i.e., $\tau_{SPU} = 100\%$). The BS is fitted with either the WiFi or the GPRS link depending on the deployment (the duty cycle of the link not present in the BS is 0).

The values of P_{SPU}, P_{BS}, P_{WiFi} and P_{GPRS}, together with τ_{SPU}, τ_{BS}, τ_{WiFi}, τ_{GPRS} and N allow us to evaluate the energy consumption of the whole system in each cycle (fixed at 60 minutes for both deployments, yet this is a parameter that can be remotely changed):

$$E_{sys} = 3600 \cdot \left(N \cdot P_{SPU} \cdot \tau_{SPU} + P_{BS} \cdot \tau_{BS} + P_{\{WiFi/GPRS\}} \cdot \tau_{\{WiFi/GPRS\}}\right) \quad (1)$$

The energy E_{batt} (in J) stored by a new lead-acid battery can be roughly estimated as:

$$E_{batt} = CH_{nm} \cdot V_{nm} \cdot 1hour \quad (2)$$

where CH_{nm} and V_{nm} are the electric charges transferred by the battery in one hour and the nominal voltage of the battery, respectively. Thus, to identify the minimum number of batteries able to guarantee at least h_{min} hours without any solar energy harvesting, we must satisfy the bound:

$$\frac{N_{batt} \cdot E_{batt}}{E_{sys}} > h_{min} \quad (3)$$

where N_{batt} is the number of batteries, in a parallel configuration. The selection of the number of solar panels for each deployment requires information about the solar radiation in the deployment area. We run a 3 months acquisition campaign of solar radiation information in winter by means of two ad-hoc embedded systems, each fitted with a nominal 20W solar panel. Let T be the time horizon of the acquisition campaign and let's consider an energy harvesting circuitry as the one presented in Figure 11, the energy (in J) acquired by one solar panel is:

$$E_{sp} = \int_T V_s(t) I_c(t) dt \quad (4)$$

where $V_s(t)$ and $I_c(t)$ are the voltage of solar panel and the current from the DC/DC regulator at time t, respectively. Let E_{sys}^T be the energy consumption of the system in the time horizon T,

$$E_{sys}^{T} = \int_{T} \left(N \cdot P_{SPU} \cdot \tau_{SPU} + P_{BS} \cdot \tau_{BS} + P_{\{WiFi/GPRS\}} \cdot \tau_{\{WiFi/GPRS\}} \right) dt. \quad (5)$$

Thus, to identify the minimum number of solar panels able to guarantee the requested long-term energy sustainability for the system we need:

$$N_{sp} \cdot E_{sp} > E_{sys}^{T} \quad (6)$$

where N_{sp} is the number of solar panels. An energy-wise effective system design requires the definition of N_{batt} and N_{sp}.

7. EXPERIMENTAL RESULTS

The rock collapse forecasting application is presented in Subsection 7.1, while current deployments are given in Subsection 7.2; Subsection 7.3 describes the system design energy-wise. Finally, Subsection 7.4 introduces and discusses the system performance in terms of energy-efficiency, ability to deal with high sampling-rates and Quality-of-Service (QoS).

7.1. Real-world application: a monitoring system for rock collapse forecasting

Rocks collapse is one of the most dangerous and sudden natural hazards in mountain regions. This harmful event, which is generally characterised by catastrophic consequences if human settlements, transport routes or critical infrastructure systems are involved, is related to the fall of rocks or stones induced by the (partial) collapse of a rock face due to frost-defrost phenomenon, thermal stress and gravitation.

The forecasting of rock collapse nowadays represents a challenging research issue and a valuable testbed for the high frequency monitoring system proposed for several reasons. Firstly, the collapse of a rock face is critical due to the lack of clear and effective forerunners. Secondly, traditional investigation techniques (e.g., those based on strain gauge and inclinometer sensors), mainly relying on data loggers, cannot be used for real-time decision making. Thirdly, the possibility to forecast a collapse in a rock is related to the availability of internal information associated with micro acoustic/seismic activities induced, at the microscopic level, by the creation and organisation of fractures from small to large dimensions.

MEMS accelerometers and geophones are the right sensors to be used for acquiring micro-acoustic signals (a micro acoustic emission is similar to a small earthquake generated within the rock face). Herein, we considered a 2kHz sampling rate since the designed system was able to support such a frequency, thus being able to detect signals up to 1kHz in bandwidth. A high synchronism among the acquisition units, not exceeding 1ms in skew, is required to carry out the localisation of the emission source. In addition to a 3 axis accelerometer or geophone, each SPU mounts traditional sensors such as strain gauge, inclinometers and temperature sensors. The SPU unit is hosted in the metallic case described in Section 4.4 and shown in Figure 13.

7.2. Current deployments: the St. Martin mount and the Rialba's tower

Currently, we have had two monitoring systems operational for more than two years on the Alps, in northern Italy: the first one on the St. Martin mount, the second one on the Rialba's towers (both on the Lake Como area). Another deployment has been recently done in Switzerland. For all deployments, geologists and geophysicists investigated the areas to identify the number and location for the SPUs. Moreover, due to the presence of metallic units, cables, and antennas, we positioned lightning rods close to the units to complement and integrate the internal lightning protections.

Fig. 13. A mounted SPU case.

(a) St. Martin mount (b) Rialba's towers

Fig. 14. The deployment areas at the St Martin mount and Rialbas towers

The St. Martin mount is a 300m high rockface near the city of Lecco, which experienced a 15000m^3 rock collapse in 1969 causing 7 fatalities. The monitoring system, which consists of eight SPUs with a different sensor platform (6 MEMS accelerometers, 2 geophones, 2 strain gauges, 8 temperature sensors, 8 MEMS inclinometer sensors) and a BS, has been active since April 1st, 2010. The BS is equipped with a 5GHz WiFi radio link with a directional antenna oriented towards our Intelligent Embedded System lab (which is located at Lecco's Campus of Politecnico di Milano) at a distance of approximately 2.5Km. The total length of the wired segments accounts for 100m connected with a CanBUS modality set to 250Kbs.

The second deployment area is the Rialba's towers, a limestone-conglomerate rock divided by a system of fractures. The towers are close to the main civil infrastructures connecting Lecco and Sondrio provinces (speedway, railway, gas and electric distribution networks). The monitoring system consists of three SPUs and a BS and has been active since July 7th, 2010. The base station relies on a UMTS modem for remote data and commands communication with our Intelligent Embedded System lab.

(a) A SPU with a geophone (b) A SPU with a strain gauge

Fig. 15. Current deployments.

7.3. Design of the system from the energy viewpoint

To correctly dimension each deployment energy-wise, in terms of number of batteries and solar panels, we used the methodology presented in Section 6 by taking into account the different number of units per system (which is application-dependent) and the different technologies considered for the long-range communication (i.e., WiFi for the system at the St. Martin mount and GPRS for the one at Rialba's towers). The power consumption of each SPU P_{SPU}, of the BS P_{BS} and the long-range radio link P_R for both deployments are given in Table IV; Table V shows the duty-cycles of SPUs τ_{SPU}, BS τ_{BS} and long-range radio link τ_R. It is noted that SPUs must be always operational (continuous data acquisition and processing) and cannot be switched off (i.e., $\tau_{SPU} = 100\%$).

Table V. Duty-cycle (%) for SPU, BS and long-range radio link and number of SPUs in the deployments

Deployment	τ_{SPU}	τ_{BS}	τ_R	N
St. Martin mount	100	16.6	1.6	8
Rialba's towers	100	16.6	3.6	3

The values of P_{SPU}, P_{BS} and P_R, together with τ_{SPU}, τ_{BS}, τ_R and N allow us to evaluate the energy consumption of the whole system in each cycle (fixed at 60 minutes for both deployments, but this parameter may be changed remotely) by using Eq. 1. These energy consumptions are summarised in Table VI; Figure 16 shows the time-profile of the power consumption per cycle for both deployments.

Table VI. Energy consumption (kJ) in a cycle (60 mins)

Deployment	Energy consumption (kJ)
St. Martin mount	10.3
Rialba's towers	7.0

We dimensioned both deployments to survive at least 10 days without any energy harvesting (i.e., $h_{min} = 240$ hours). By using Eq. 3 and considering a standard lead-acid battery (e.g., $V_{nm} = 12V$, $CH_{nm} = 30Ah$), we obtained $N_{batt} = 2$ batteries for both systems. It is worth noting that with such dimensioning, we had the system survive to 15 days of continuous rain thanks to the MPPT energy harvester, which was able to

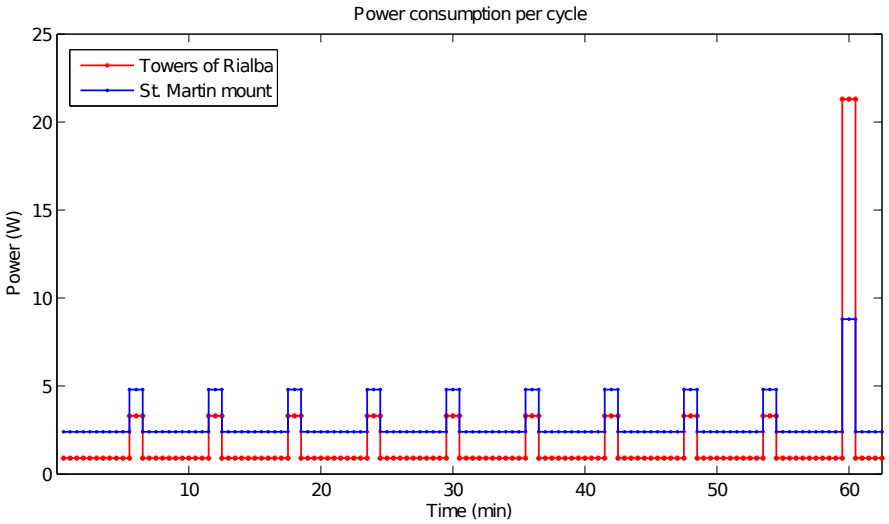

Fig. 16. Time-profile of the power consumption per cycle (60 mins) for both deployments.

extract up to 3W (for a 20W nominal panel) even on cloudy days (e.g., see 'bad weather' in Figure 18).

The selection of the number of solar panels for each deployment required a detailed design phase. As described in Section 6, we started with a long-term acquisition campaign of solar radiation information lasting 3 months (i.e., $T = 3$ months) in winter by means of two ad-hoc embedded systems fitted with a nominal 20W solar panel. These data, together with a detailed model of both the energy harvesting circuitry and the power consumption of the systems considered, allowed us to select $N_{sp} = 3$ nominal 20W solar panels for the system at the St. Martin mount and $N_{sp} = 2$ nominal 20W solar panels for the Rialba's towers.

7.4. Measurements from the deployments

We provide the real data to show the energy sustainability of the systems (by looking at solar-generated power and the battery voltage), the capability to sample up to 2kHz (by looking at an acquired burst both in time and frequency domain) and the QoS (by looking at the uptimes of the system units). In more detail, the solar generated power and the voltage of the batteries for the July 2010-July 2011 period are given in Figure 17 for the Rialba's towers system. The data, which refer to one solar panel and one battery, show the system capability to keep the battery voltage always above 12V for the entire one-year period.

Figure 18 shows a detail of Figure 17 by presenting the harvested power and the battery voltage between December 11, 2010 and January 13, 2011. This figure is particularly interesting since the period considered includes two time slots of consecutive bad weather conditions. In more detail, from December 21 to December 27 the solar panels did not acquire any energy due to heavy rainfalls. The battery voltage decreased from 13V to approximately 12V but the system was able to keep all of its functionalities active (i.e., acquisition, processing and remote transmission). Afterwards, some sunny days allowed the battery voltage to recover. Likewise, the period between January, 4th and January, 13th was characterised by bad weather conditions causing the battery voltage to drop again. The acquisition measurements of January, 3rd 2011 are interesting and show the capability of the MPPT board (as stated in Section 5.2) to har-

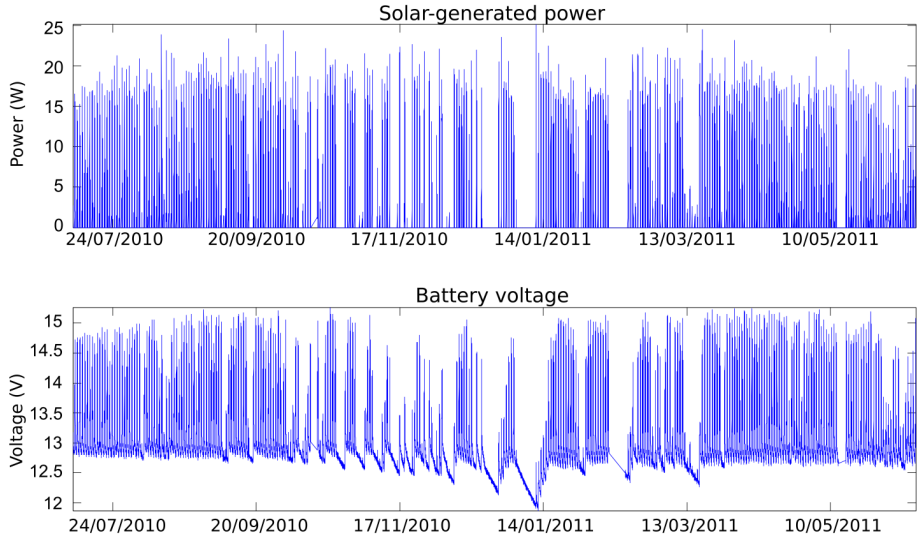

Fig. 17. The generated solar power and the voltage of the battery for the period July 2010- July 2011, Rialba's towers : a) generated solar power b) battery voltage

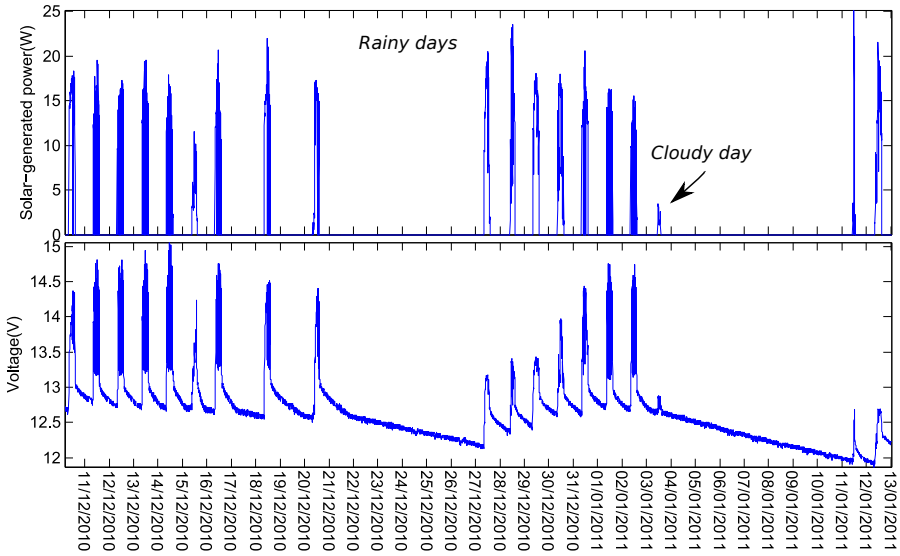

Fig. 18. A detail of the generated solar power and the voltage of the battery for the period December 11th, 2010- January 13th, 2011, Rialba's towers: a) generated solar power b) battery voltage.

vest even small quantity of energy when available (see the small peaks in the battery voltage).

Figure 19 presents the average solar generated power per month for both the solar panels in the July 2010-June 2011 period. In 2011 in northern Italy we experienced an

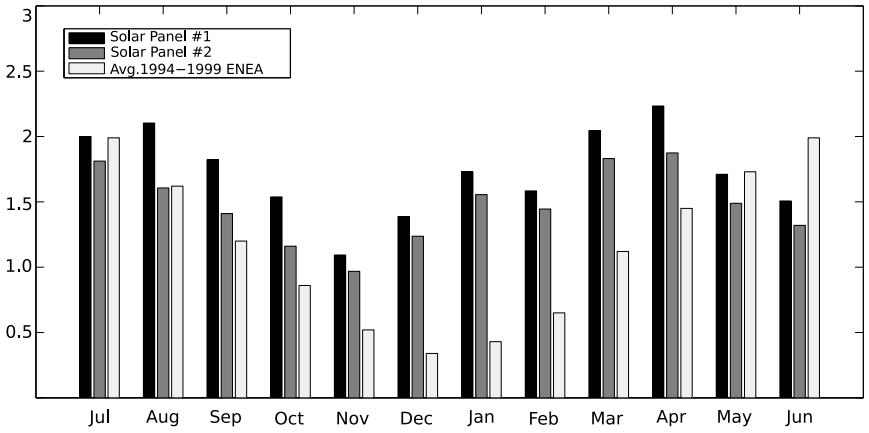

Fig. 19. Average acquired solar generated power per month for the period July 2010- June 2011 .

exceptionally sunny and hot April and a very bad June, which is well reflected by the very high value of generated power in April 2011 compared to that of May and June.

We compared the average solar generated power acquired per month to the value provided by ENEA (Italian National agency for new technologies, Energy and sustainable economic development) in the same area of the deployments during the years 1994-1999 [ENEA 1999]. To compute these values we considered a solar panel as being the same size as the ones we considered and a panel efficiency equal to 0.3. The expected results are in line with the generated power acquired by our system. The differences between the expected and the measured solar power could be ascribed to the specific position and orientation of the solar panel considered and to the fact that our measurements are related to a single year (while ENEA data are averaged over five years). Having this in mind, data from ENEA can be safely used to dimension any other deployment needs without carrying out a preliminary, in-situ investigation.

Figure 20 shows an example of a burst detected by the system at the Rialba's towers during its monitoring activity. In particular, Figures Figures 20(a), 20(c) and 20(e) detail the three accelerometer output components (X, Y and Z) of the acquired burst. As expected by geologists and geophysicists, the analysis in the Fourier domain, presented in Figures 20(b), 20(d) and 20(f), shows that the signal frequencies of the bursts range from 400Hz to 900Hz. A more detailed analysis of the acquired burst is presented in the companion paper [Alippi et al. 2012].

To evaluate the QoS of the proposed system we considered the uptime counter for the SPUs and the BSs in both deployments (these data logs are sent together with sensed data to the control room). Such analysis allows us to identify possible long-term, non devastating bugs not recognisable through laboratory tests.

To measure the uptime counter of a BS, we rely on a counter of the duty cycles (a timestamp is associated with each value of the counter). Since the duty-cycling period is regular (e.g., five minutes), the corresponding plot is a line (whose slope is directly affected by the duty cycle). Figure 21 shows the counters from the BSs of both the deployments. In the St. Martin mount deployment we can observe an irregular behaviour: the counter reset three times in the first six months and four times in the first year of the deployment.

The reason is due to a corruption of the file system caused by a software bug in the code running on the BS and blocking the system. We had to reformat the USB pen drive to reactivate the system. In June 2011, we modified the duty cycle of the

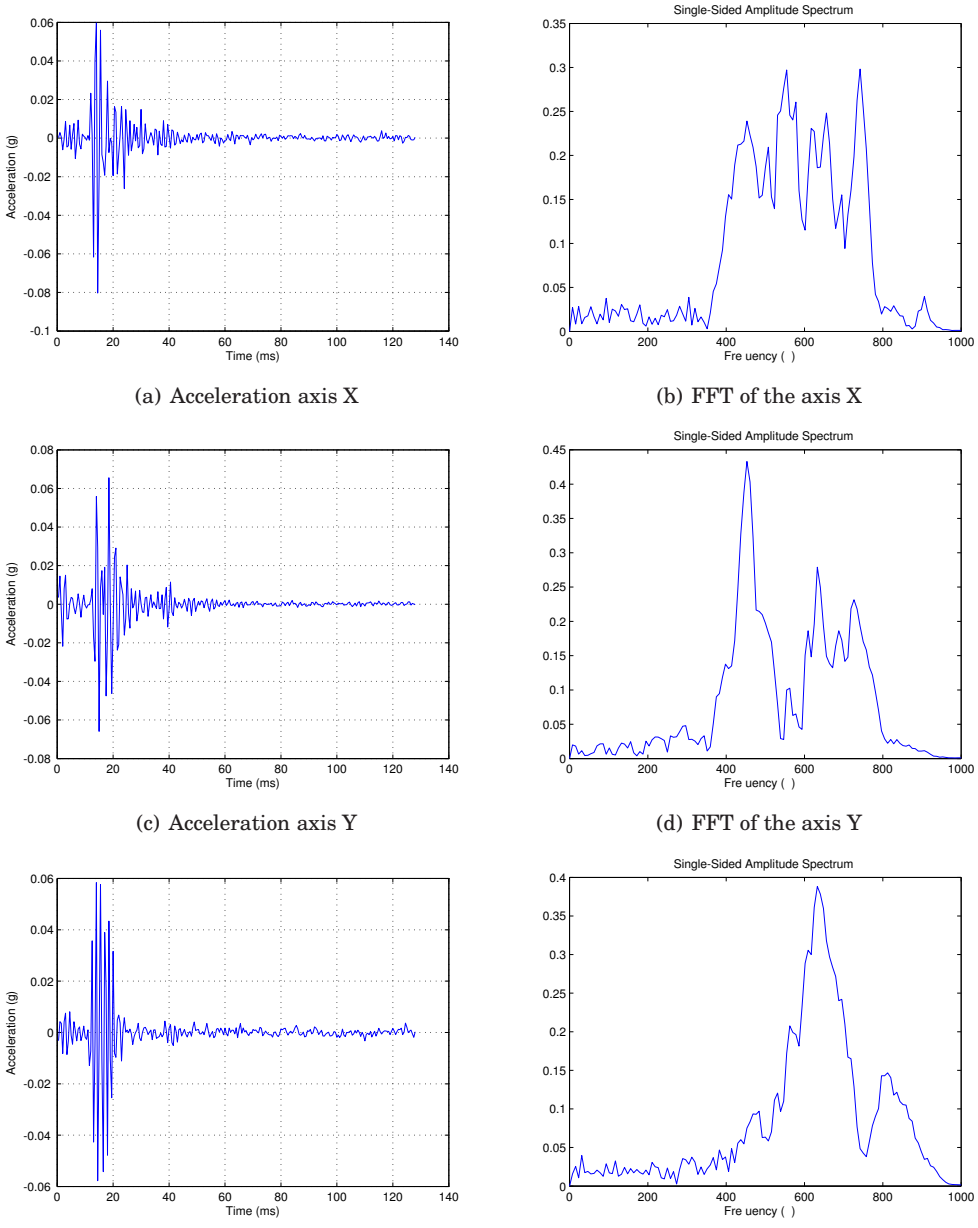

(a) Acceleration axis X

(b) FFT of the axis X

(c) Acceleration axis Y

(d) FFT of the axis Y

(e) Acceleration axis Z

(f) FFT of the axis Z

Fig. 20. An example of a detected burst (X,Y and Z components) and its Fourier plot

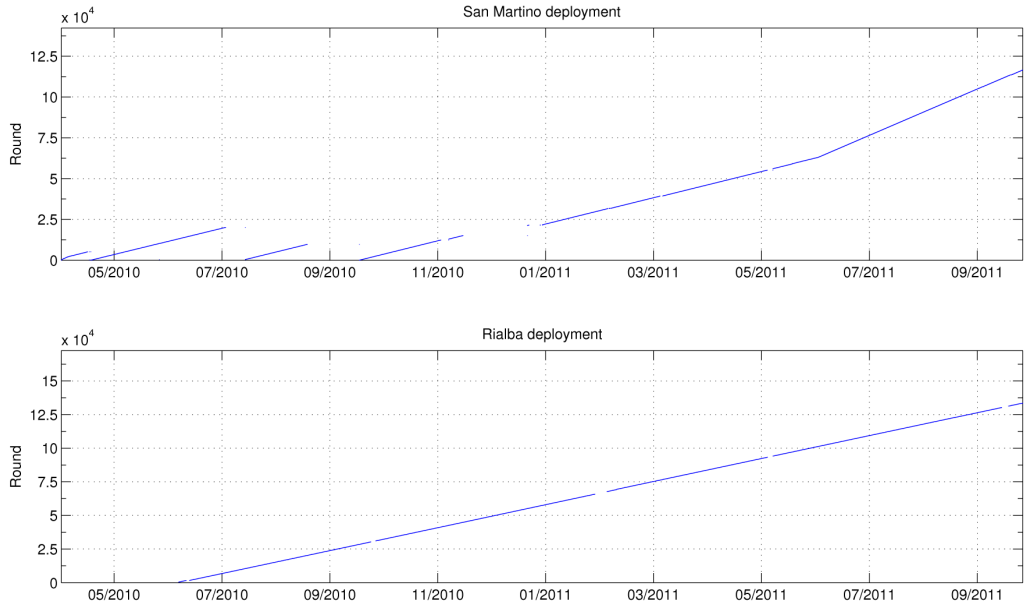

Fig. 21. BS uptime counter over time

Table VII. Deployment QOS

Deployment	*Deployment duration(days)*	*QOS(%)*
St. Martin mount	534	84.1
Rialba's towers	471	96.7

BS at the St. Martin's deployment to 2.5 minutes, as explained by the change in the line slope. The Rialba's towers system is an evolution of the system deployed at the St. Martin mount where the software bug causing the file system problem has been fixed. This resulted in a significant improvement of the QoS. In particular, Figure 21 demonstrates shows that the reliability of the Rialba's towers system largely improved compared to that at the St. Martin mount since the counter never reset. In Table VII, we summarise the QoS for the two systems in terms of total uptime counter w.r.t. the deployment duration up to October 2011. It is worth noting that both the system at the St. Martin mount and the Rialba's towers underwent a data loss in the counter plot. This was due to a software bug on the server software of the control room: in particular, an unhandled exception caused the abnormal termination of the thread responsible for saving the gathered data to the database, causing the data loss.

In addition to the QoS of the BSs, we evaluated the uptime counters of the SPUs to take into account possible soft-resets (e.g., caused by the watch dog timer) or communication timeouts (e.g., due to communication problems). To this end, we rely on two 16-bit counters provided by the FreeRTOS operating system, named `tick` and `overflows`. The first one is incremented every OS ticks, the latter when the counter `tick` overflows. Then, the corresponding uptime counter is computed as $\texttt{overflows} * 2^{16} + (\texttt{tick}/500)$. When both `overflows` and `tick` counters overflow, the corresponding uptime counter restarts at zero. Moreover, these counters reset to zero after every node reset because they are stored to the RAM. In particular, Figure 22 presents the uptime counters of Node 1 and 4 deployed in St. Martin mount (the other units provide similar results and their uptime counters are omitted for brevity), while Figure 23 shows the uptime counter for Rialba's towers units. It is noted that in all the plots, the uptime counter

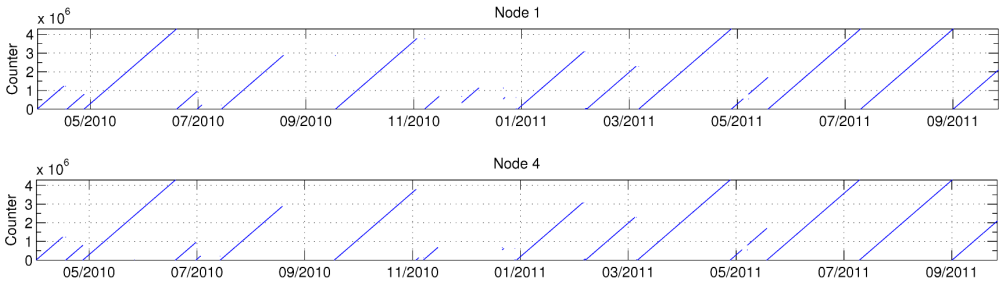

Fig. 22. St. Martin mount: uptime counters of Nodes 1 and 4.

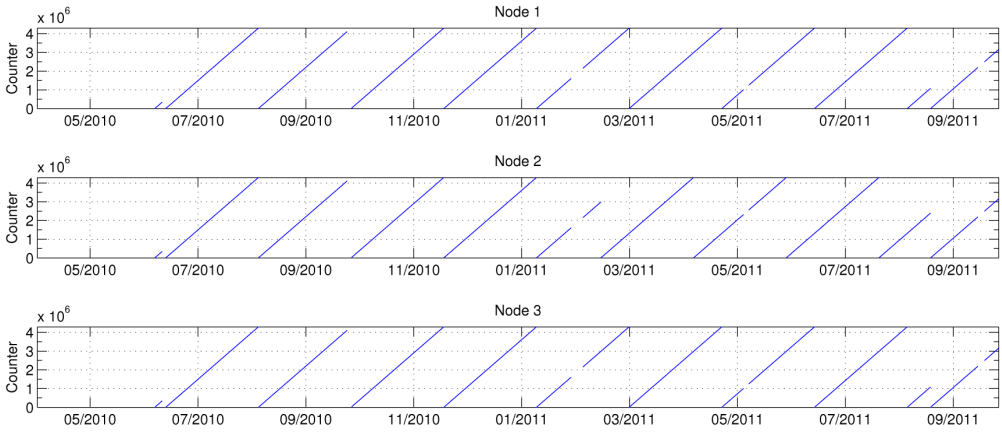

Fig. 23. Rialba's towers: uptime counters of deployed nodes.

overflows frequently, meaning that no soft-reset or communication timeouts occurred. In particular, the deployment at Rialba's towers is not affected by these types of faults (the corresponding uptime counter always reaches its maximum value). On the contrary, the SPUs at the St. Martin mount experienced resets induced by problems at the BSs (due to the randomly activating software bugs). In addition, in February and June 2011 the counters of all the SPUs at the St. Martin mount reset to zero for maintenance actions on the BSs. Table VIII shows the QoS for each node of the two deployments.

8. CONCLUSIONS

The hardware design of a hybrid wireless-wired monitoring system for high-frequency sampling has been presented in this paper. Unlike the solutions found in the literature, the chosen architecture and the ad-hoc designed electronics guarantee both long-term system availability (by means of energy efficient policies and energy harvesting mechanisms) and flexibility and adaptability to changes in the network, environment or application requirements (through a remote reconfigurability of the units). The effectiveness of the proposed monitoring system has been tested in a challenging monitoring application for the forecasting of rock collapse, an application characterised by strict constraints such as high sampling rate (up to 2kHz), high synchronisation among the acquisition units (down to 0.5 ms) and difficulties in the energy harvesting. Two deployments have been presented in this paper, which have been active in remote harsh environments on the Alps for almost two years.

Table VIII. Per node QOS

Net	*Node*	*QOS(%)*
St. Martin mount	1	84,5
	2	82,9
	3	82,9
	4	83,1
	5	84,8
	6	84,8
	7	84,8
	8	84,8
Rialba's tower	1	97.0
	2	97.0
	3	96.1

ACKNOWLEDGMENTS

The authors would like to sincerely thank Prof. Gourab Sen Gupta, Massey University, New Zealand, for the precious help in improving the quality of the manuscript.

REFERENCES

AKYILDIZ, I., SU, W., SANKARASUBRAMANIAM, Y., AND CAYIRCI, E. 2002. A survey on sensor networks. *Communications Magazine, IEEE 40,* 8, 102–114.

ALIPPI, C., BORACCHI, G., CAMPLANI, R., MARULLO, A., AND ROVERI, M. 2012. An hybrid monitoring system for the real-time processing of high frequency data. part a: Software aspects. Tech. rep. Internal Report.

ALIPPI, C., CAMPLANI, R., AND GALPERTI, C. 2007. Lossless compression techniques in wireless sensor networks: Monitoring microacoustic emissions. In *Robotic and Sensors Environments, 2007. ROSE 2007. International Workshop on*. IEEE, 1–5.

ALIPPI, C., CAMPLANI, R., GALPERTI, C., MARULLO, A., AND ROVERI, M. 2010. An hybrid wireless-wired monitoring system for real-time rock collapse forecasting. In *Mobile Adhoc and Sensor Systems (MASS), 2010 IEEE 7th International Conference on*. IEEE, 224–231.

ALIPPI, C. AND GALPERTI, C. 2008. An adaptive system for optimal solar energy harvesting in wireless sensor network nodes. *IEEE Transactions on Circuits and Systems I: Regular Papers 55,* 6, 1742–1750.

BASHARAT, A., CATBAS, N., AND SHAH, M. 2005. A framework for intelligent sensor network with video camera for structural health monitoring of bridges. In *Pervasive Computing and Communications Workshops, 2005. PerCom 2005 Workshops. Third IEEE International Conference on*. IEEE, 385–389.

BOLLER, C., CHANG, F., AND FUJINO, Y. 2009. *Encyclopedia of Structural Health Monitoring*. Wiley.

CAICEDO, J., MARULANDA, J., THOMSON, P., AND DYKE, S. 2002. Monitoring of bridges to detect changes in structural health. In *American Control Conference, 2001. Proceedings of the 2001*. Vol. 1. IEEE, 453–458.

CROSSBOW. 2009. `http://www.xbow.com/`.

DELL'ACQUA, A., HANSEN, M., IKINEN, S., LOFSTEDT, B., VANUXEM, J., SVENSSON, C., YUAN, J., HENTZELL, H., DEL BUONO, L., DAVID, J., GENAT, J., LEBBOLO, H., LEDORTZ, O., NAYMAN, P., SAVOY-NAVARRO, A., ZITOUN, R., ALIPPI, C., BREVEGLIERI, L., DADDA, L., PIURI, V., SALICE, F., SAMI, M., STEFANELLI, R., CATTANEO, P., FUMAGALLI, G., GOGGI, G., BRIGATI, S., GATTI, U., MALOBERTI, F., TORELLI, G., CARLSON, P., KEREK, A., APPELQUIST, G., BERGLUND, S., BOHM, C., ENGSTROM, M., YAMDAGNI, N., SUNDBLAD, R., HOGLUND, I., AND PERSSON, S. 1993. System level policies for fault tolerance issues in the fermi project. In *Defect and Fault Tolerance in VLSI Systems, 1993., The IEEE International Workshop on*. 1 –8.

EISENMAN, S., MILUZZO, E., LANE, N., PETERSON, R., AHN, G., AND CAMPBELL, A. 2009. Bikenet: A mobile sensing system for cyclist experience mapping. *ACM Transactions on Sensor Networks (TOSN) 6,* 1, 6.

ENEA. 1999. http://clisun.casaccia.enea.it/pagine/tabelleradiazione.htm. In *Tabella della Radiazione Solare, ENEA - Italian National agency for new technologies, Energy and sustainable economic development*.

ENGEL, J., ZHAO, L., FAN, Z., CHEN, J., AND LIU, C. 2004. Smart brick-a low cost, modular wireless sensor for civil structure monitoring. In *International Conference on Computing, Communications and Control Technologies (CCCT 2004), Austin, TX USA*.

FARRAR, C., PARK, G., AND TODD, M. 2011. Sensing network paradigms for structural health monitoring. *New Developments in Sensing Technology for Structural Health Monitoring*, 137–157.

FARRAR, C. AND WORDEN, K. 2007. An introduction to structural health monitoring. *Philosophical Transactions of the Royal Society A: Mathematical, Physical and Engineering Sciences 365,* 1851, 303.

GLASER, S. 2005. Terra-Scope: a MEMS-based vertical seismic array. *Proc. SPIE*.

GRATTAN, S., TAYLOR, S., BASHEER, P., SUN, T., AND GRATTAN, K. 2009. Structural health monitoring-better solutions using fiber optic sensors? In *Sensors, 2009 IEEE*. IEEE, 811–814.

GUNGOR, V. AND HANCKE, G. 2009. Industrial wireless sensor networks: Challenges, design principles, and technical approaches. *Industrial Electronics, IEEE Transactions on 56,* 10, 4258–4265.

HU, W., BULUSU, N., CHOU, C., JHA, S., TAYLOR, A., AND TRAN, V. 2009. Design and evaluation of a hybrid sensor network for cane toad monitoring. *ACM Transactions on Sensor Networks (TOSN) 5,* 1, 4.

INGELREST, F., BARRENETXEA, G., SCHAEFER, G., VETTERLI, M., COUACH, O., AND PARLANGE, M. 2010. Sensorscope: Application-specific sensor network for environmental monitoring. *ACM Transactions on Sensor Networks (TOSN) 6,* 2, 17.

JOHNSON, W., AULD, B., AND ALERS, G. 1994. Spectroscopy of resonant torsional modes in cylindrical rods using electromagnetic-acoustic transduction. *The Journal of the Acoustical Society of America 95*, 1413.

KIM, S., PAKZAD, S., CULLER, D., DEMMEL, J., FENVES, G., GLASER, S., AND TURON, M. 2007. Health monitoring of civil infrastructures using wireless sensor networks. In *Proceedings of the 6th international conference on Information processing in sensor networks*. ACM, 254–263.

LAWRENZ, W. 1997. *Can System Engineering: From Theory to Practical Applications* 1st Ed. Springer-Verlag New York, Inc., Secaucus, NJ, USA.

LIM, S. AND SHOURESHI, R. 2003. Neural-based monitoring system for health assessment of electric transmission lines. In *American Control Conference, 2003. Proceedings of the 2003*. Vol. 3. IEEE, 2270–2275.

LIM, S. AND SHOURESHI, R. 2006. Advanced monitoring system for integrity assessment of electric power transmission lines. In *American Control Conference, 2006*. IEEE, 6.

LYNCH, J., LAW, K., KIREMIDJIAN, A., CARRYER, E., FARRAR, C., SOHN, H., ALLEN, D., NADLER, B., AND WAIT, J. 2004. Design and performance validation of a wireless sensing unit for structural monitoring applications. *Structural Engineering and Mechanics 17,* 3-4, 393–408.

LYNCH, J., PARTRIDGE, A., LAW, K., KENNY, T., KIREMIDJIAN, A., AND CARRYER, E. 2003. Design of piezoresistive MEMS-based accelerometer for integration with wireless sensing unit for structural monitoring. *Journal of Aerospace Engineering 16*, 108.

MARÓTI, M., KUSY, B., SIMON, G., AND LÉDECZI, A. 2004. The flooding time synchronization protocol. In *Proceedings of the 2nd international conference on Embedded networked sensor systems*. ACM, 39–49.

MOTEIV. 2007. Tmote invent. `http://www.moteiv.com/`.

PAEK, J., CHINTALAPUDI, K., CAFFREY, J., GOVINDAN, R., AND MASRI, S. 2005. A wireless sensor network for structural health monitoring: Performance and experience.

PAEK, J., GREENSTEIN, B., GNAWALI, O., JANG, K., JOKI, A., VIEIRA, M., HICKS, J., ESTRIN, D., GOVINDAN, R., AND KOHLER, E. 2010. The tenet architecture for tiered sensor networks. *ACM Transactions on Sensor Networks (TOSN) 6,* 4, 34.

RAMAMURTHY, H., PRABHU, B., GADH, R., AND MADNI, A. 2007. Wireless industrial monitoring and control using a smart sensor platform. *IEEE Sensors Journal 7,* 5, 611–618.

RICE, J. AND SPENCER JR, B. 2008. Structural health monitoring sensor development for the Imote2 platform. In *Proceedings of the SPIEThe International Society for Optical Engineering*. Vol. 6932. 693234–1.

RICE, J. AND SPENCER JR, B. 2009. Flexible smart sensor framework for autonomous full-scale structural health monitoring. *Newmark Structural Engineering Laboratory Report Series 018*.

SCHMID, J., G\\"ADEKE, T., STORK, W., HENNRICH, H., AND BLANK, T. 2010. A wireless MEMS-sensor network concept for the condition monitoring of ball screw drives in industrial plants. In *Proceedings of the 8th ACM Conference on Embedded Networked Sensor Systems*. ACM, 425–426.

SISGEO. 2012. Home page. `http://www.sisgeo.com/`.

SOLGEO. 2012. Home page. `http://www.solgeo.eu/`.

WERNER-ALLEN, G., LORINCZ, K., WELSH, M., MARCILLO, O., JOHNSON, J., RUIZ, M., AND LEES, J. 2006. Deploying a wireless sensor network on an active volcano. *IEEE Internet Computing*, 18–25.